Nonlinear Dyn (2014) 78:2459–2477
DOI 10.1007/s11071-014-1603-y

ORIGINAL PAPER

Stability and response of a self-amplified braking system under velocity-dependent actuation force

Li Chen · Gang Xi

Received: 30 December 2013 / Accepted: 14 July 2014 / Published online: 19 August 2014

Abstract Wedge brakes, featuring self-amplification, inspire good opportunity to obtain large normal force by small actuation force. A single degree of freedom torsional model with harmonic excitation for a driveline with a wedge brake is developed to investigate the effect of velocity-dependent actuation force. The stability analysis indicates that instability can occur even with a constant friction coefficient and is greatly influenced by the slope of the actuation force. Three bifurcation points are found: one stable, one unstable, and the other one Hopf. Phase portraits, time domain responses, Poincaré maps, and frequency spectra are provided by nonlinear computation. Three motions are observed: unidirectional stick-slip, bidirectional stick-slip, and non-stick-slip. Due to the self amplification, the wedge brake leads to more stick motions and more side bands compared with the conventional brake. By varying the slope, the dynamic response of the driveline can be synchronous or irregular multi-periodic motion. The dynamics at negative slope is studied further considering three other influencing factors, i.e., the initial actuation force, excitation frequency, and wedge angle. The results are provided by the comparison with those of the driveline with a conventional brake.

L. Chen (✉) · G. Xi
National Lab of Automotive Electronics and Control,
Shanghai Jiao Tong University, Shanghai 200240, China
e-mail: li.h.chen@sjtu.edu.cn

Keywords Wedge mechanism · Self-amplified · Braking dynamics · Nonlinear

1 Introduction

Friction brakes, stopping motions by friction interfaces, are widely used in vehicle braking systems [1], automatic transmissions [2], and etc. Wedge brakes, featuring self-amplification, can generate large friction force by small actuation force [3]. Resultantly, wedge brakes can be energy saving and space saving. Feasibility studies have been conducted for wedge brake applications, such as eBrake [4,5], automatic manual transmission [6], and clutch-to-clutch shift transmission [7]. The results show wedge brakes have great potential to replace conventional friction brakes. However, as we know, friction interfaces tend to introduce nonlinear dynamics to braking systems [8], involving intractable vibration problems [9]. So, we need to concern irregular dynamics and its engineering significance for wedge brakes.

Wedge brakes do not change the intrinsic friction, however, change the ratio of the friction force over actuation force. For the conventional brake, the normal force, though determined by external forces, can be considered as an active actuation force for the friction interface. The ratio of the friction force over normal force is defined as the friction coefficient, which is symmetric about the origin as described in the Coulomb friction model [10]. However, for the wedge brake, the

normal force is passive, because it is generated by an actuation force acting on one side surface of the wedge. Derived from force equilibrium of the wedge, the ratio of the friction force over actuation force is associated with the wedge geometry other than the motion direction and friction coefficient [7]. On the one hand, the ratio is greatly amplified compared with the friction coefficient. On the other hand, the ratio is asymmetric about the origin; specifically, the ratio at forward motion can be several ten times that at backward motion. Intuitively, this extreme asymmetry induces special stick-slip motion and even irregular dynamic response.

Extensive researches on friction-induced dynamics have been already conducted for classical friction interfaces [11,12]. Nonlinear phenomena have been discovered in numerical and experimental results, such as stick-slip motions [13,14], limit cycles [15,16], bifurcations [17,18], and chaotic motions [19,20]. Friction characteristics [19], mechanical system parameters [9], excitation amplitude and frequency [21] and friction interface deformation [22] are factors inducing nonlinear dynamics, which is unexpected in automotive powering [23,24], braking [9] and other areas [25]. Naturally, these inducing factors also affect dynamics of wedge brakes. And, due to the asymmetric characteristic, dynamic response may be much different. The stability of wedge brake system is related to the difference between the wedge angle and friction coefficient [26]. Unfortunately, no further publication is found on the wedge brake dynamics, which will be necessary consideration when the wedge brake is applied in real system. So this paper aims to expose unique nonlinear dynamics for wedge brakes.

Another point is noticed that the normal force is usually considered as a constant in the aforementioned studies on conventional friction-induced dynamics. However, the normal force is a major control input and is velocity dependent in close-loop control [24,27]. In the well-known braking squeal or groan problem, braking vibration is initiated during the process of braking manipulation [28], which means, the effect of the normal force profile is not negligible. In the wedge brake, the normal force is generated by the actuation force with the asymmetric amplification ratio, and the actuation force can be a velocity-dependent control input. Despite the well-known conclusion that a negative slope in the friction characteristic leads to instability and self-excitation [19,23], this paper focuses on the effect of varying actuation force on wedge brake dynamics even with constant kinetic friction coefficient.

Friction brakes are commonly modeled as multibody systems [13,29] or using finite element methods [30,31] resulting in models with high numbers of degrees of freedom (DOF). Nevertheless, for a basic understanding of the excitation mechanism and the influence of system parameters, and for active control of brake vibration, models with a low number of DOF are more convenient, such as the 3DOF model [32] and 2DOF model [33]. Single DOF (SDOF) models are also widely used for dry friction oscillator under constant belt velocity and harmonic driving force [34] and for stability and local bifurcation behavior of the exponential friction model [35]. Chaotic motions, stick-slip motions, and period doubling phenomena are observed in a SDOF oscillator [36]. Taking the wedge actuation mechanism into consideration, a new SDOF torsional model is established in this paper to study the dynamics behavior of the driveline under actuation of the wedge brake.

The goal of this paper was to examine factors influencing stability and dynamic response of the driveline actuated by the wedge brake under velocity-dependent actuation force. The dynamic behavior is demonstrated by comparing against that of the driveline actuated by a conventional brake. The rest of the paper is organized as follows. The SDOF model is described in Sect. 2; the evolution of the root locus and vibration mode is illustrated for stability analysis using the linear method in Sect. 3. Further, a smoothening method is employed for nonlinear analysis, followed by numerical results and discussion in Sect. 4. Finally, the conclusion is given in Sect. 5.

2 Analytical model

The brake decelerates the motion of the driveline by applying friction force. The SDOF torsional model with both dry friction and viscous damping elements is illustrated in Fig. 1a, where J denotes the moment of inertia of the driveline, k and c denote the stiffness and viscous damping, T is the external torque of the driveline, and θ is the angular displacement. The brake actuation force F_a is applied on the short edge of the wedge, which generates the friction force F_μ on the friction interface between the wedge and the friction surface of the driveline.

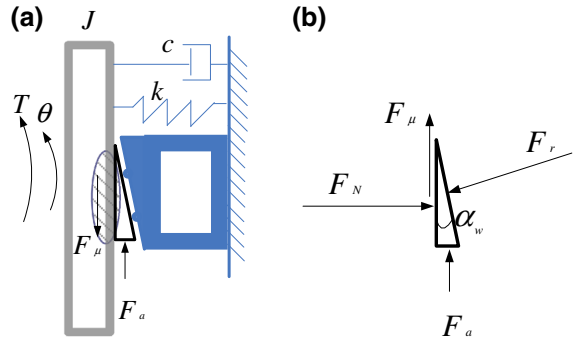

Fig. 1 Model of the driveline with a wedge brake **a** SDOF model, **b** force equilibrium

The governing equation is

$$J\ddot{\theta}(t) + c\dot{\theta}(t) + k\theta(t) + RF_{\mu}(t) = T(t), \tag{1}$$

where R is the equivalent radius of the friction force F_{μ}. The force equilibrium of the wedge is illustrated in Fig. 1b and is expressed mathematically as

$$\left(F_{\mu} + F_a\right)/F_N = \tan(\alpha_w). \tag{2}$$

The action force F_a is assumed to be a function of the relative velocity $\dot{\theta}(t)$ and defined as

$$F_a(t) = F_{a0} + \delta \cdot abs\left(\dot{\theta}(t)\right), \tag{3}$$

where δ is the slope of F_a, and F_{a0} is the value of F_a at $\delta = 0N \cdot$ s/rad. The external torque T on the driveline is assumed to be a harmonic function as $T = T_e \cdot \sin(2\pi \cdot f_e \cdot t)$, where f_e is the cyclical frequency.

Given kinetic friction coefficient μ_k and static friction coefficient μ_s, a Coulomb friction model is used to describe F_{μ} as

$$F_{\mu} = \begin{cases} F_N \cdot \mu_k \cdot sign(\dot{\theta}(t)) & \dot{\theta}(t) \neq 0 \\ [-F_N \cdot \mu_s F_N \cdot \mu_s] & \dot{\theta}(t) = 0 \end{cases} \tag{4}$$

Substitution of (4) into (2) yields the following expression of F_{μ} under the condition of $\tan(\alpha_w) > \mu_k$. The case of $\tan(\alpha_w) < \mu_k$ is not studied in this paper for it results in instability and is not recommended in the wedge mechanism design [26].

$$F_{\mu} = \begin{cases} F_a \cdot \mu_k \cdot \text{sign}(\dot{\theta}(t)) / \left(\tan(\alpha_w) - \mu_k \cdot \text{sign}(\dot{\theta}(t))\right) & \dot{\theta}(t) \neq 0 \\ [-F_a \cdot \mu_s / (\tan(\alpha_w) - \mu_s)\ F_a \cdot \mu_s / \tan(\alpha, ,_w) - \mu_s] & \dot{\theta}(t) \neq 0 \end{cases} \tag{5}$$

Thus, the calculation of F_{μ} is segmented into three parts for $\dot{\theta}(t) > 0$, $\dot{\theta}(t) < 0$ and $\dot{\theta}(t) = 0$, respectively. The driveline under brake described in (1) crosses the three segments; therefore, the nonlinear system is piecewise linear in terms of the direction of $\dot{\theta}(t)$. The actuation force F_a affects the stability of the linearized system under the two cases, $\dot{\theta}(t) > 0$ and $\dot{\theta}(t) < 0$, which are investigated in detail in the following section.

3 Stability analysis

To examine the stability, define the physical system by the following state equation where $\mathbf{X} = [x_1 x_2]^{\mathrm{T}}$ is the state variable vector, $\mathbf{A}$ is the system matrix, and $\mathbf{U}$ is the input vector.

$$\dot{\mathbf{X}} = \mathbf{A}\mathbf{X} + \mathbf{U}. \tag{6}$$

Here,

$$x_1(t) = \theta(t),\ x_2(t) = \dot{\theta}(t) \tag{7}$$

Parameters are selected as follows: $J = 1\ \text{kg m}^2$, $k = 10{,}000\ \text{N m/rad}$, $c = 1\ \text{N ms/rad}$, $\mu_k = 0.30$, $\mu_s = 0.33$, $R = 0.2$ m. The cyclical natural frequency is $f_n = 15.91$ Hz.

From (1), (3), (5) and (7), the system matrix $\mathbf{A}$ and input vector $\mathbf{U}$ are derived as

$$\mathbf{A} = \begin{pmatrix} 0 & 1 \\ -\frac{k}{J} & -\frac{c}{J} - \frac{R\cdot\delta\cdot\mu_k}{J(\tan(\alpha_w) - \mu_k \cdot sign(x_2(t)))} \end{pmatrix}, \tag{8}$$

$$\mathbf{U} = \begin{pmatrix} 0 \\ \frac{T(t)}{J} - \frac{R\cdot F_{a0}\cdot\mu_k\cdot\text{sign}(x_2(t))}{J(\tan(\alpha_w) - \mu_k\cdot\text{sign}(x_2(t)))} \end{pmatrix}. \tag{9}$$

Note that the friction force is split into two parts in $\mathbf{A}$ and $\mathbf{U}$, respectively: one is associated with a state variable, namely damping, and the other is considered as an independent external force. For stability analysis, where the force term in the control input expression (9) is not considered, the characteristic equation becomes

$$\det\begin{pmatrix} \lambda & -1 \\ \frac{k}{J} & \lambda + \frac{c}{J} + \frac{R\cdot\delta\cdot\mu_k}{J(\tan(\alpha_w) - \mu_k\cdot\mathbf{sign}(x_2(t)))} \end{pmatrix} = 0 \tag{10}$$

where, λ is the eigenvalue of the matrix $\mathbf{A}$. Define the natural frequency $\omega_n = \sqrt{k/J}$ and a symbol h as following, the solution of λ is calculated by:

$$h = -\left(\frac{c}{2J} + \frac{R\cdot\delta\cdot\mu_k}{2J\cdot(\tan(\alpha_w) - \mu_k\cdot sign(x_2(t)))}\right) \tag{11}$$

$$\lambda = h \pm \sqrt{h^2 - \omega_n^2} \tag{12}$$

The asymptotically stable criterion is a negative real part of λ. Since $\tan(\alpha_w) < \mu_k$ is not an interested case

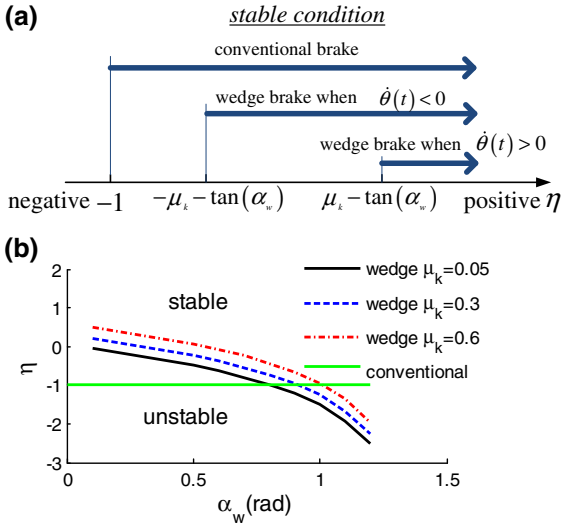

Fig. 2 Summary of stability criterions

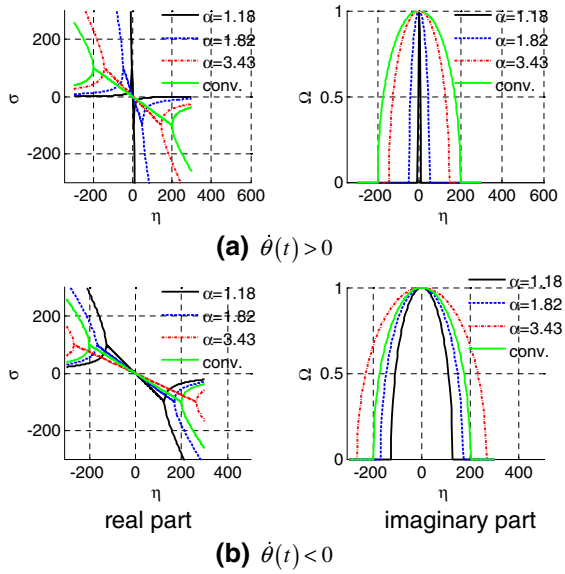

Fig. 3 Evolution of the eigenvalue

of this study as explained before, the stable criterion for $\tan(\alpha_w) > \mu_k$ is derived as:

$$\frac{\delta \cdot R \cdot \mu_k}{c} > \mu_k \cdot sign(x_2(t)) - \tan(\alpha_w) \tag{13}$$

Normalized parameters are used to illustrate numerical results. The friction damping is normalized as defined by $\eta = (\delta \cdot R \cdot \mu_k)/c$. Define eigenvalues as $\lambda = \sigma \pm i\omega$. The imaginary parts are normalized with respect to the natural frequency, denoted by $\Omega = \omega/\omega_n$. The wedge angle α_w is normalized with respect to the kinetic friction coefficient μ_k, defined as $\alpha = \tan(\alpha_w)/\mu_k$.

For the convenience of comparison, the conventional brake is analyzed by giving the SDOF model, linearized state equation, and stable condition in Appendix. The stability criteria in terms of η are summarized in Fig. 2. As seen from Fig. 2a, the critical $\eta = -\mu_k - \tan(\alpha_w)$ when $\dot{\theta}(t) < 0$ for the wedge brake is less than the critical $\eta = \mu_k - \tan(\alpha_w)$ when $\dot{\theta}(t) > 0$, so the stable condition $\eta > \mu_k - \tan(\alpha_w)$ is the intersection of the two cases. This condition is illustrated numerically in Fig. 2b.

Two differences are observed between the wedge and conventional brake (1). As seen from Fig. 2a, the critical η is a constant as -1 for the conventional brake; however, it is varying along the friction coefficient μ_k and the wedge angle α_w for the wedge brake (2). As seen from Fig. 2b, small μ_k or large α_w expands the stable area of the wedge brake compared that of the conventional brake; large μ_k or small α_w shrinks the stable area. In order to gain large amplification ratio, the wedge angle is always designed to be greater but close to $\arctan(\mu_k)$ [7]. Thus, the value of $\mu_k - \tan(\alpha_w)$ is a bit negative but close to zero, and definitely larger than -1. So the stable area of the wedge brake is less than that of the conventional brake, which means, the conventional brake can tolerate more negative slope of the actuation force.

Further, the solution format of λ in (27) is the same as that in (12), which means, their eigenvalue evolutions are similar, though, not identical. Due to the asymmetric characteristic of the wedge brake, the evolutions are different for $\dot{\theta}(t) > 0$ and $\dot{\theta}(t) < 0$, illustrated in Fig. 3a and b, respectively. For the purposes of easy comparison, the evolutions of the conventional brake are plotted in Fig. 3a and b; actually, they are the same because of the symmetric characteristics.

The eigenvalue real parts for $\dot{\theta}(t) > 0$ are plotted in Fig. 3a where both stable (negative σ) and unstable (positive σ) are clearly seen. This stability analysis indicates that instability can occur even with a constant friction coefficient and is greatly influenced by η and accordingly δ, no matter for the wedge brake or for the conventional brake. The normalized wedge angle α does not affect the wedge brake stability significantly; however, it affects the evolution rate. Large α gains slow rate. Nevertheless, the evolution rate of the conventional brake is slower than that of the wedge brake.

Two bifurcation points are detected for each case in the evolution map. The vibration mode collapses when η is less than the left bifurcation point. As η increasing, a vibration mode appears until η arrives at the right bifurcation point, and then, the vibration mode disappears again. Other than those, one Hopf bifurcation point is detected for each wedge brake case at $\eta = \mu_k - \tan(\alpha_w)$ for it divides stable and unstable zones by a limit cycle. For the conventional brake, the Hopf bifurcation point is at $\eta = -1$.

The vibration mode and bifurcation points are similarly detected for $\dot{\theta}(t) < 0$ as shown in Fig. 3b. However, the evolution rates of Ω and σ for the wedge brake are much slower than those for $\dot{\theta}(t) > 0$. Extremely, the rate at $\alpha = 3.43$ is slower than that of the conventional brake. In addition, the vibration mode exists in a wider range of η.

Figures 2 and 3 show positive η tends to fall into the stable area; whereas, negative η tends to the unstable area. Therefore, non-positive η is the focus of following section on nonlinear analysis.

4 Nonlinear computation

Although the linear analysis in the previous section is useful, it does not provide detailed information on the nonlinear dynamical behavior of the system. For example, the studied problem has nonlinear external inputs which are not expressed in the system matrix **A**. As a matter of fact, these signum function inputs have damper-like function which helps the system to be more stable or less unstable. Since nonlinear analysis accounts for all the linear and nonlinear terms to decide whether the system is stable or not, it is possible for linear analysis to predict an unstable system, but the results may be stable because of the damper-like facts.

Two more normalized variables other than η and α are used for the analysis. The external torque $T(t)$ is a harmonic function of t with amplitude T_e and frequency f_e. The initial actuation force F_{a0} is normalized with respect to an equivalent external force, defined as $F_0 = F_{a0}/\left(T_e/(\mu_k \cdot R)\right)$. The frequency f_e is normalized with respect to the natural frequency f_n, defined as $f = f_e/f_n$.

The friction force expressed in (5) shows discontinuity at zero relative velocity, which leads to inconvenience for numerical computation. In order to overcome the computational difficulty, smoothening functions are explored [37], and one simple expression is employed as below [38]:

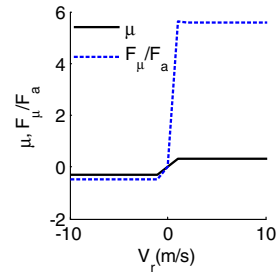

Fig. 4 Smoothened friction characteristics

$$\mu(v_r) = \left[1.0 + \left(\frac{\mu_s}{\mu_k} - 1.0\right) e^{-\varsigma \cdot abs(v_r)}\right] \cdot \tanh(\xi \cdot v_r) \tag{14}$$

in which v_r is the relative speed on the friction interface, ς and ξ are two tuning parameters. The calculation of v_r is

$$v_r = R \cdot \dot{\theta}(t). \tag{15}$$

The value of μ is calculated as shown in Fig. 4, given $\varsigma = 6$ and $\xi = 100$. Besides F_μ/F_a is derived from (5) by the substitution of μ_k with μ of (14). The value is also plotted in Fig. 4 at $\alpha = 1.03$. F_μ/F_a reaches 5.58 when $v_r > 0$, however, reaches 0.46 when $v_r < 0$. Thus, the former is 12 times the latter. The amplification ratio becomes larger when α approaches 1 [7], and vice versa.

One example with stick-slip motion is given in Fig. 5 to show the comparison of the numerical results between the Coulomb friction model and the smoothened model in (14). The numerical calculation of F_μ in (5) for the Coulomb friction model is derived as below:

$$F_\mu = \begin{cases} F_{\mu\_\max} & \dot{\theta}(t) > \varepsilon \\ F_{\mu\_\min} & \dot{\theta}(t) < -\varepsilon \\ sat(F_s) & -\varepsilon \le \dot{\theta}(t) \le \varepsilon \end{cases} \tag{16}$$

in which ε is a small positive number with the value 10^{-4} in the simulation, and

$$F_{\mu\_\max} = F_a \cdot \mu_k / (\tan(\alpha_w) - \mu_k), \tag{17}$$

$$F_{\mu\_\min} = -F_a \cdot \mu_k / (\tan(\alpha_w) + \mu_k), \tag{18}$$

$$F_s = \left(T(t) - J\ddot{\theta}(t) - c\dot{\theta}(t) - k\theta(t)\right)/R \tag{19}$$

$$sat(F_s) = \begin{cases} F_{\mu\_\max} & F_s > F_{\mu\_\max} \\ F_s & F_{\mu\_\min} \le F_s \le F_{\mu\_\max} \\ F_{\mu\_\min} & F_s < F_{\mu\_\min} \end{cases} \tag{20}$$

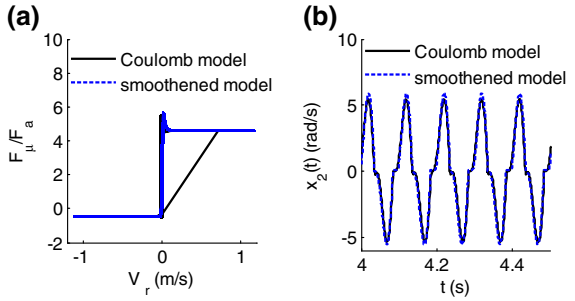

Fig. 5 Comparison between smoothened and Coulomb friction model ($\eta = 0,\ f = 0.63,\ F_0 = 0.09,\ \alpha = 1.21$) **a** friction characteristics, **b** angular velocity

The computation is implemented in MATLAB/SIMULINK. The solver configurations for the two models are the same, which use ODE14X(extrapolation) with fixed fundamental sample time as 10^{-4}s and the extrapolation order as 4.

It can be seen from Fig. 5a that the two models generate identical values of F_μ / F_a when v_r is away from zero, and the smoothening function approaches the Coulomb model well in a continuous way when v_r approaches zero. As seen from Fig. 5b, the dynamic responses calculated from the two models behave obvious stick–slip motions and match each other well. Therefore, although no mathematical proof is given that the smoothening function is correct, it seems to give accurate results.

Nevertheless, there are two differences between the two models regarding to numerical calculation. First, the calculation of the smoothened model takes 7.6 s (for the example case with 5 s simulation time), and

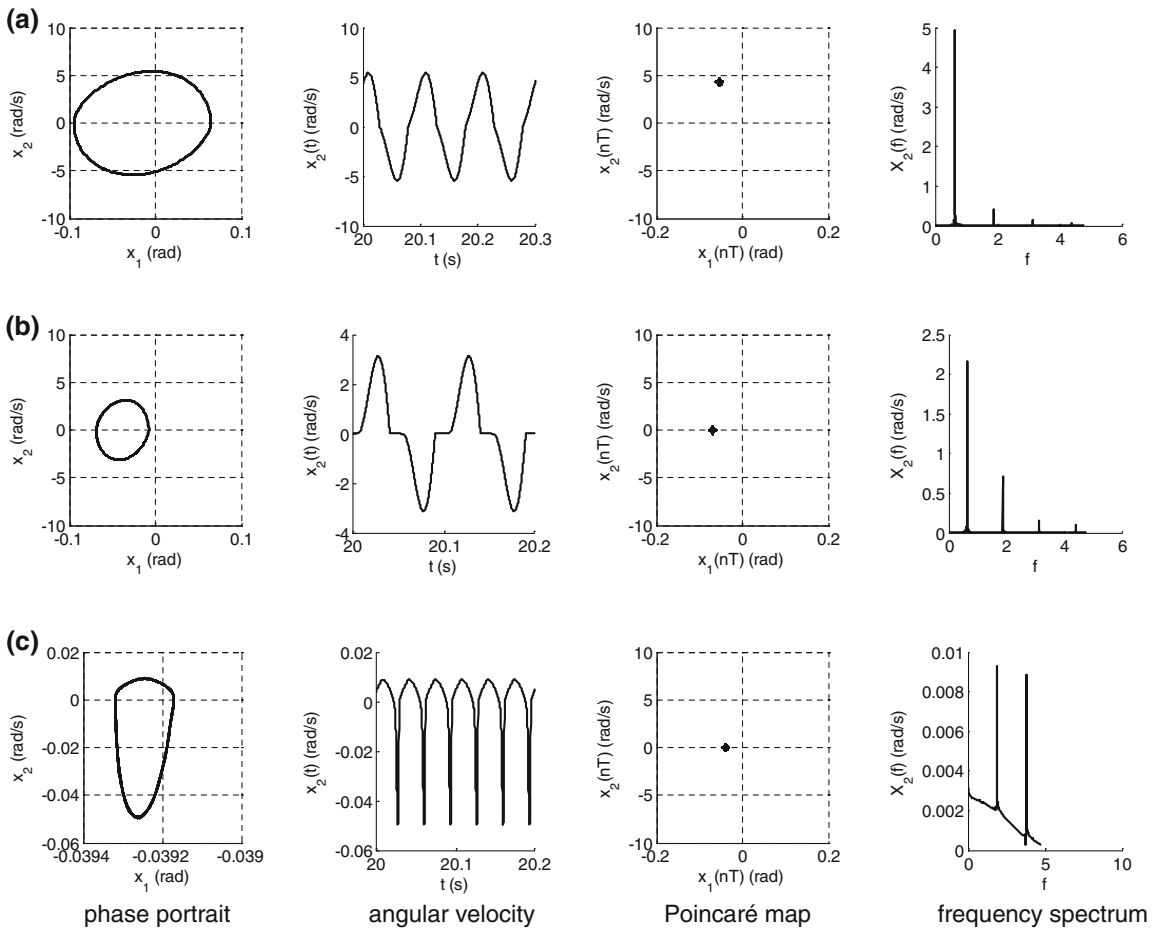

Fig. 6 Stick-slip motions of the driveline with the wedge brake at $\eta = 0$. **a** non-stick-slip motion at $f = 0.63,\ F_0 = 0.1200, \alpha = 1.18$, **b** bidirectional stick-slip motion at $f = 0.63,\ F_0 = 0.09, \alpha = 1.18$, **c** unidirectional stick-slip motion at $f = 1.89,\ F_0 = 0.114, \alpha = 1.18$

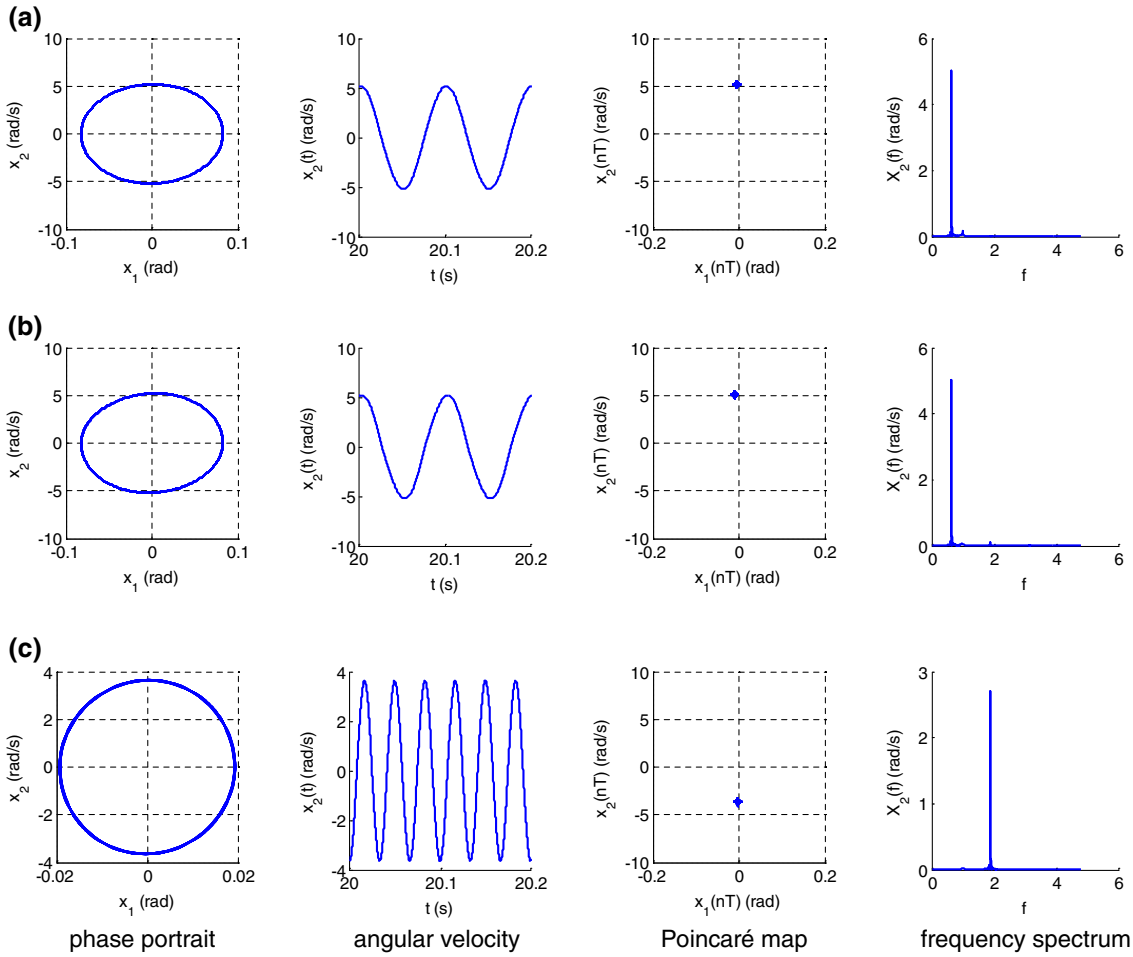

Fig. 7 Motions of the driveline with the conventional brake at $\eta = 0$. (**a**) motion at $f = 0.63,\ F_0 = 0.1200, \alpha = 1.18$ (**b**) motion at $f = 0.63,\ F_0 = 0.09, \alpha = 1.18$ (**c**) motion $f = 1.89,\ F_0 = 0.114, \alpha = 1.18$

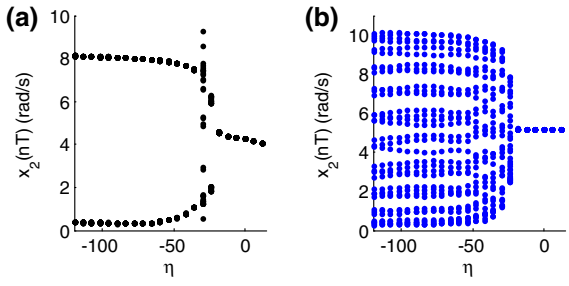

Fig. 8 Bifurcation diagrams of $x_2\,(nT)$ gversus normalized slope η of actuation force. **a** wedge brake and **b** conventional brake

that of the Coulomb model takes 15.1 s. So the former is much shorter than the latter. Second, the calculation of the Coulomb model tends to be out of convergent for small α or large F_a due to the discontinuity, while the calculation of the smoothened model works well. Since this paper will examine the dynamic behavior of the self-amplified braking system in wide ranges of parameter variations, the smoothening function in (14) is employed for the nonlinear computation.

The numerical results firstly demonstrate three typical motions observed in the driveline with the wedge brake, i.e., unidirectional stick-slip, bidirectional stick-slip, and non-stick-slip. Then, the numerical computation investigates the effect of η on driveline dynamics using a bifurcation diagram. The results provide phase portraits, time domain responses, Poincaré maps, and frequency spectra. Since $\eta < 0$ introduces more complicated dynamics, the dynamics at $\eta < 0$ is studied further considering three influencing factors, i.e., F_0, f, and α. The values of the varying parameters

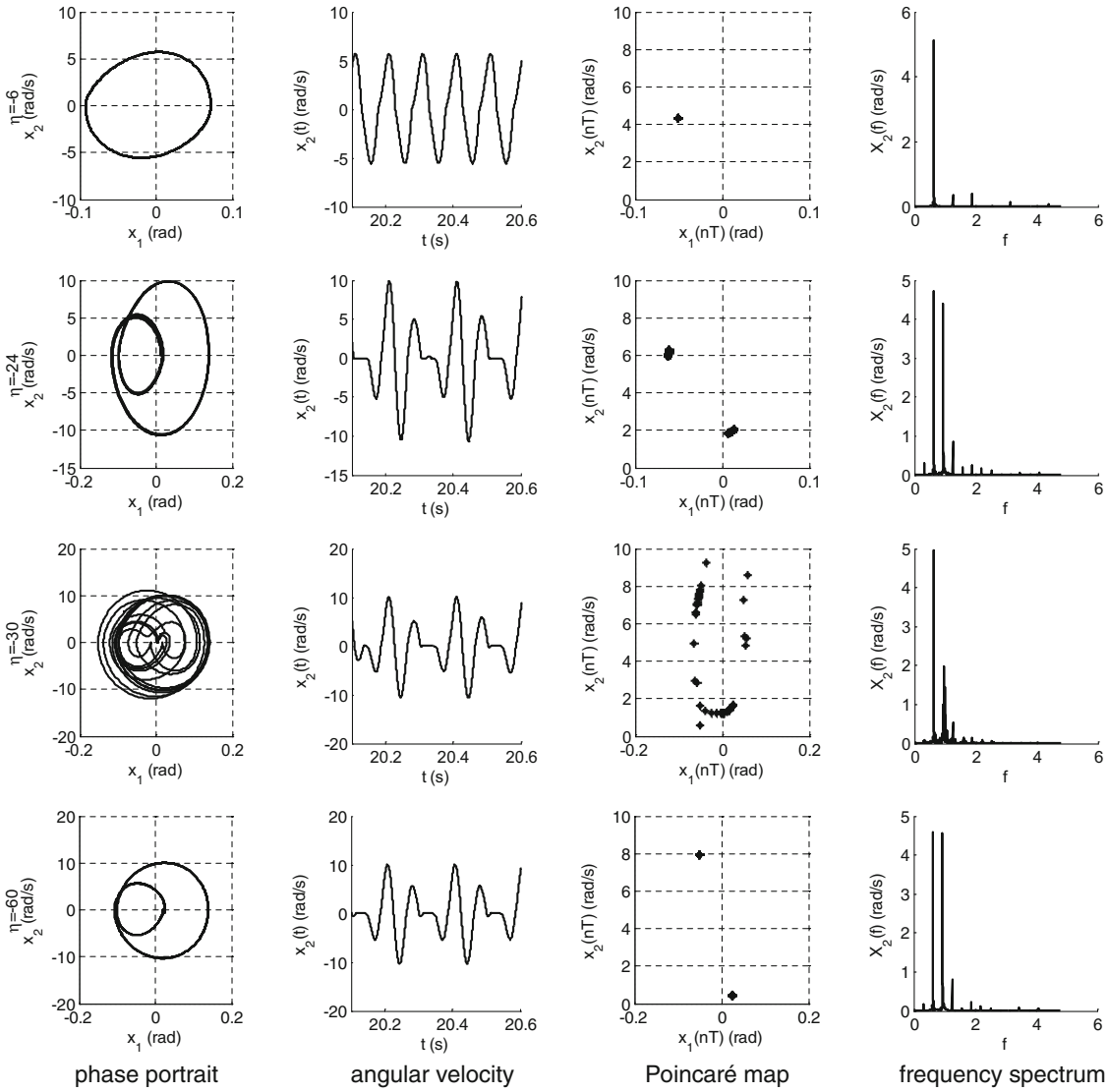

Fig. 9 Dynamic responses with different η at $f = 0.63,\ F_0 = 0.036,\ \alpha = 1.18$ for wedge brake

are selected according to the segments in the bifurcation diagrams. For each case, the nonlinear dynamic behavior of the driveline with the conventional brake is computed and compared with the same parameter values.

All data throughout the 25 s running time of the model are memorized and utilized to generate the dynamic responses and frequency spectra. And the last 5s data are utilized to generate the phase portraits, the Poincaré maps, and the bifurcation diagrams.

The time domain responses and the phase portraits can be easily obtained as the time series of the angular displacement and angular velocity of the driveline are memorized in the calculation procedure. A Poincaré section, on which the points of the time series are at the constant time interval $T_t (T_t = 1/f_e)$, is selected to get the Poincaré map. In this paper, the angular velocity of the driveline at $t_1,\ t_1 + T_t,\ t_1 + 2T_t, \ldots, t_1 + 5 \cdot f_e \cdot T_t$ is memorized and plotted on the Poincaré map. t_1 is the time at which the oscillation of the driveline has already reached stable, and it is selected as 20s for the cases studied in this paper.

To generate the bifurcation diagram, the obtained points on the Poincaré map are used with a certain

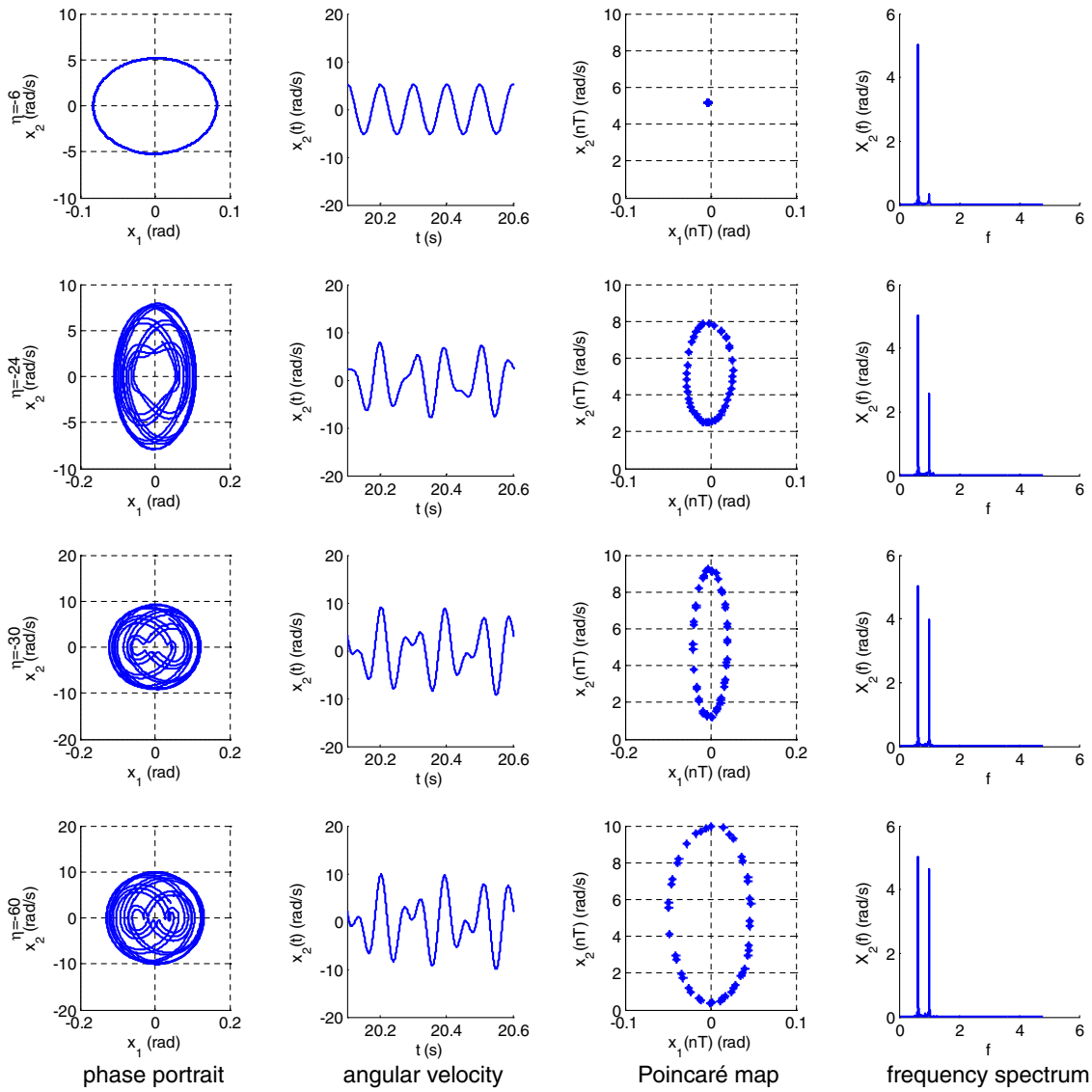

Fig. 10 Dynamic responses with different η at $f = 0.63$, $F_0 = 0.036$, $\alpha = 1.18$ for conventional brake

varying parameter as the bifurcation parameter. In this paper, the actuation force slope η, initial actuation force F_0, external torque frequency f and the wedge angle α are selected as the bifurcation parameters, respectively.

4.1 Stick-slip motions

Three types of stick-slip motion are observed in the driveline with the wedge brake, illustrated in Fig. 6. For comparison, the motions of the driveline with the conventional brake are given in Fig. 7.

The non-stick-slip motion crosses the zero velocity point without a stop. It can be seen from the time domain response of Fig. 6a that the rate of the angular velocities of the driveline with the wedge brake before and after the zero velocity points is distorted, unlike the smoothness of that with the conventional brake as shown in Fig. 7a. The phase portrait in Fig. 6a also expresses the distortion. The frequency spectrum of the driveline with the wedge brake contains more side bands at other than the external torque frequency, however, that with the conventional friction brake concentrates on the external torque frequency.

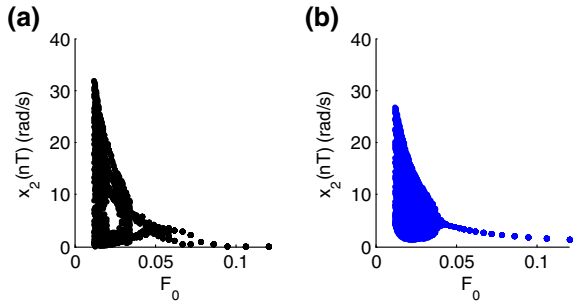

Fig. 11 Bifurcation diagrams of $x_2\,(nT)$ gversus normalized initial actuation force F_0. (**a**) wedge brake and (**b**) conventional brake

Bidirectional stick-slip motion has been reported in the many literatures on friction-induced dynamics [28] and is also found in the driveline with the wedge brake. By decreasing F_0, the results are plotted in Fig. 6b. It is observed that the edge from negative to zero velocity is much quicker than that from zero to negative, and the edge from zero to positive is milder than that from positive to zero. This asymmetry differs from normal bidirectional stick-slip motions under harmonic excitation. The frequency spectrum contains side bands other than the external torque frequency. For the driveline with the conventional brake, the decreasing F_0 does not affect the dynamic response significantly, as Fig. 7b looks similar to Fig. 6a without distortion.

Unidirectional stick-slip is a unique motion found in the driveline with wedge brake by increasing f and increasing F_0, as shown in Fig. 6c. The positive angular velocities approximately equal to zero, which fall in the range of static friction in Fig. 4. These velocities are not exactly zero due to the smoothening approximation. Nevertheless, these points can be considered to be stick. On the other hand, the points with big negative angular velocity are slipping. Unlike the normal stick-slip motion which slips in both positive and negative direction, the wedge brake-induced stick-slip motion only slips at negative velocity, however, does not slip at positive velocity. The reason lies in much larger friction force at positive velocity than at negative force, as shown in Fig. 4. Besides, the frequency spectrum contains more energy in side bands due to the stick motion. For the driveline with the conventional brake, the increasing f and increasing F_0 do not introduce special stick-slip motion, only with an external excited limit cycle and a clean frequency spectrum at excitation frequency.

4.2 Effect of η

In this section, the normalized slope of the actuation force η is selected as the bifurcation parameter and varies from 12 to -120 covering the often used operation style from mild to abrupt. With an increasing η and other parameter constant, the bifurcation diagrams obtained for the wedge brake and conventional brake are shown in Fig. 8.

Figure 8a shows that the response of the driveline with the wedge brake exhibits 2T-periodic motion at large negative η ($\eta < -30$), transits to quasi-periodic motion at $\eta = -30$, after that, transits to multi-periodic motion until $\eta = -18$, and then exhibits synchronous motion when $\eta > -18$. On the other hand, Fig. 8b shows that the response of the driveline with the conventional brake exhibits quasi-periodic motion when $\eta \leq -24$ and then transits to synchronous motion when $\eta > -24$. Thus, the typical η values are selected as -6, -24, -30, and -60. The phase portraits, angular velocity, Poincaré map, and frequency spectrum for the wedge brake and conventional brake are shown in Figs. 9 and 10, respectively.

For the wedge brake, the response at $\eta = -6$ exhibits asymmetry distortions at negative or positive angular velocity, which are similar to the distortion at $\eta = 0$ in Fig. 6a. Unidirectional stick-slip motions are found in the angular velocity at $\eta = -24, -30$, and -60. When the angular velocity goes from positive to negative, a stick motion occurs; however, when the velocity goes from negative to positive, non-stick-slip occurs. The reason is more energy dissipated due to larger friction force at positive velocity compared with that at negative velocity due to the asymmetric characteristic of the wedge brake. The Poincaré map at $\eta = -30$ shows irregular multi-periodic motions. The responses at $\eta = -24$ and -60 are simpler than that of the conventional brake in Fig. 10. The frequency spectra of the wedge brake exhibit many side bands other than the natural frequency and excitation frequency.

On the other hand, the responses of the driveline with the conventional brake only exhibit non-stick-slip motions. The frequency spectra concentrate on the natural frequency and excitation frequency.

4.3 Effect of F_0 when $\eta < 0$

In this section, the normalized initial actuation force F_0 is selected as the bifurcation parameter. The value of F_0

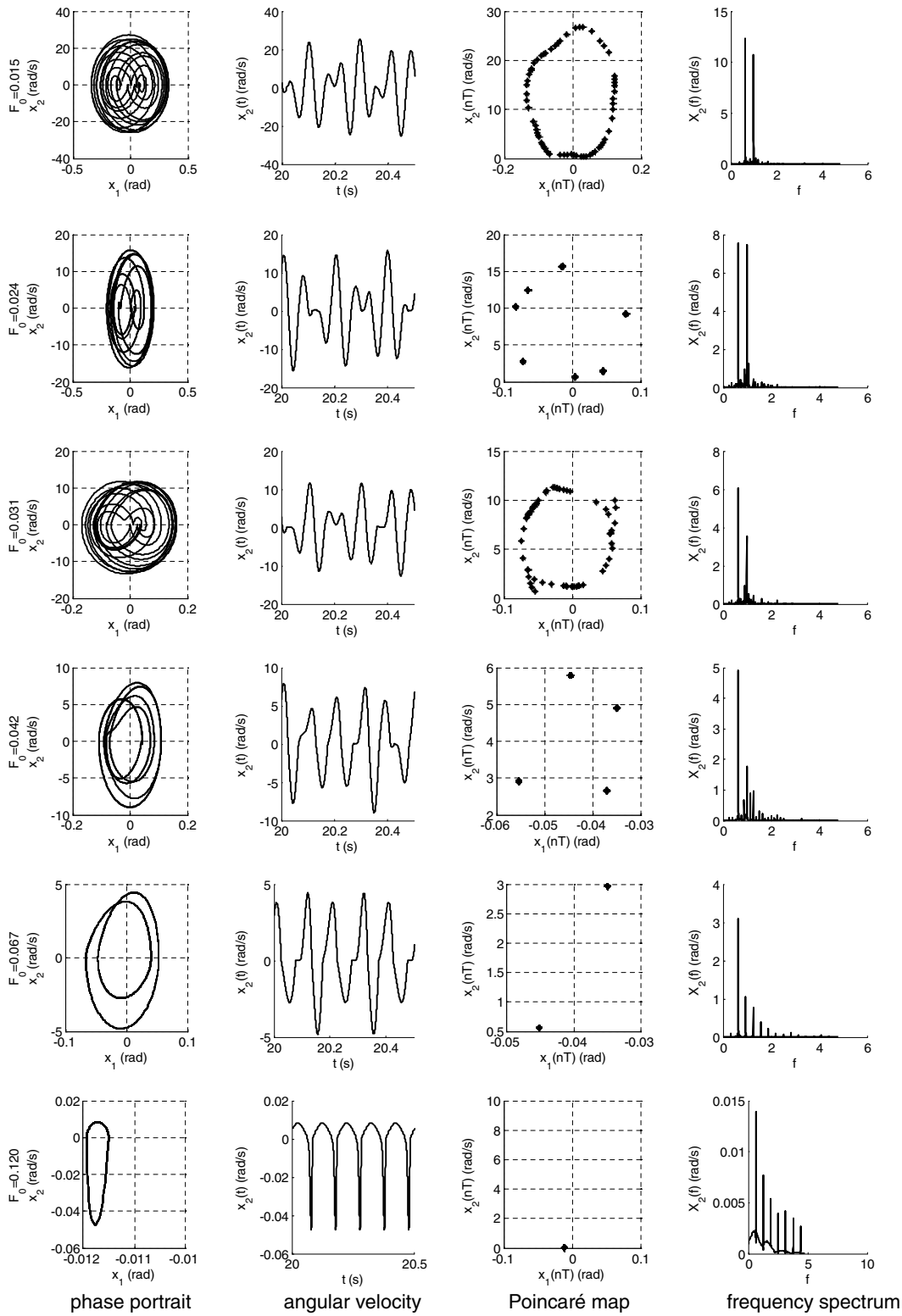

Fig. 12 Dynamic responses with different F_0 at $\eta = -24,\ f = 0.63, \alpha = 1.18$ for wedge brake

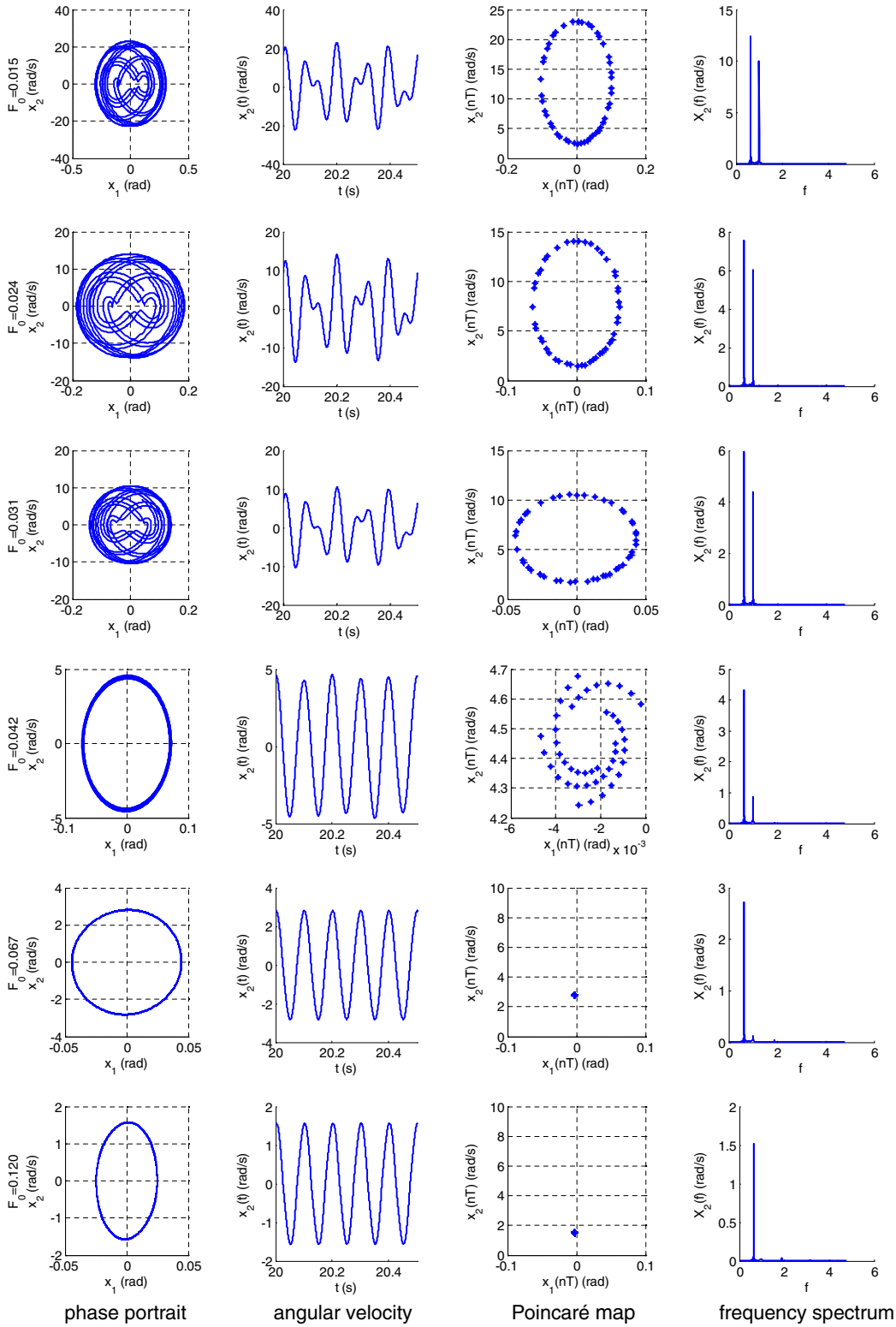

Fig. 13 Dynamic responses with different F_0 at $\eta = -24,\ f = 0.63, \alpha = 1.18$ for conventional brake

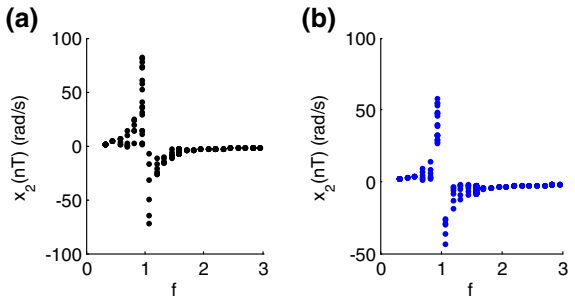

Fig. 14 Bifurcation diagrams of $x_2\,(nT)$ gversus normalized excitation frequency f **a** wedge brake and **b** conventional brake

varies from 0.012 to 0.12 (with T_e varies from 1,500 to 150 Nm at $F_{a0} = 300$ N), covering the operation from light to heavy braking. η is selected to be -24 since it represents an often used mild braking operation and induces the typical 2T-periodic motion as illustrated in Fig. 8. With an increasing F_0 and other parameter constant, the bifurcation diagrams are obtained as shown in Fig. 11.

Figure 11a indicates that the response evolution can be divided into 6 segments. The first segment exhibits quasi-periodic motion at small F_0 ($0.012 \leq F_0 \leq 0.019$). After that, the response transits to multi-periodic motion when $0.019 < F_0 \leq 0.028$, reverts to quasi-periodic motion when $0.028 < F_0 \leq 0.034$, transits to small amplitude multi-periodic motion when $0.034 < F_0 \leq 0.058$, and then, transits to 2T-periodic motion when $0.058 < F_0 \leq 0.072$, finally, transits to synchronous motion when $0.072 < F_0 \leq 0.120$. On the other hand, the response evolution of the driveline with the conventional brake in Fig. 11b can only divided into two segments. The first segment exhibits quasi-periodic motion when $0.012 \leq F_0 \leq 0.044$. After that, the motion transits to synchronous motion when $0.044 < F_0 \leq 0.120$. Therefore, the wedge brake gains synchronous motion at larger F_0 and induces more types of motion other than the quasi-periodic motion at small F_0. The phase portraits, angular velocity, Poincaré map, and frequency spectrum at $F_0 = 0.015$, 0.024, 0.031, 0.042, 0.067, and 0.120 (each falls into the 6 segments, respectively) under the two conditions are shown in Figs. 12 and 13, respectively.

At $F_0 = 0.015$, the responses of the driveline with the wedge brake and conventional brake both exhibit quasi-periodic motions. The Poincaré map for the conventional brake is a standard ellipse, however, that for the wedge brake is distorted. Other than in the quasi-periodic motion, the distortion also occurs in multi-periodic motions as shown in Fig. 12a–d.

It is observed that the three types of stick-slip motion occur along with the increasing of F_0. The response exhibits non-stick slip motion at $F_0 = 0.015$, asymmetric bidirectional stick-slip motion at $F_0 = 0.024$, 0.031, 0.042, and 0.067, and, Unidirectional stick-slip motion occurs at $F_0 = 0.120$. Further, larger F_0 comes up with more stick motion, because larger friction force is generated. Besides, more stick motions come up with more side bands in frequency spectra.

On the other hand, the responses of the driveline with the conventional brake only exhibit non-stick-slip motions. The stable duration at $F_0 = 0.042$ is longer than that at other values, nevertheless, the state variable approaches a point after a while. The frequency spectra at any of the calculated values are rather neat, concentrating on the natural frequency and excitation frequency.

4.4 Effect of f when $\eta < 0$

In this section, the normalized excitation frequency f is selected as the bifurcation parameter and varies from 0.3 to 3. With an increasing f and other parameter constant, the bifurcation diagrams are shown in Fig. 14.

Figure 14a indicates that the response evolution can be divided into 5 segments. The first segment exhibits synchronous motion at small $f\,(0.3 \leq f < 0.56)$. After that, the response transits to multi-periodic motion when $0.56 \leq f < 1$, reverts to synchronous motion at $f = 1$, again, transits to multi-periodic motion when $1 < f \leq 1.57$, and transits to synchronous motion when $1.57 < f \leq 3$. Further, the value of $x_2\,(nT)$ is positive when $f < 1$, whereas negative when $f > 1$. The response evolution in Fig. 14b for the conventional brake is similar to that in Fig. 14a. They differ in the f value at the beginning of the multi-periodic motion. The value is 0.69 for the conventional brake, compared with 0.57 for the wedge brake. The phase portraits, angular velocity, Poincaré map, and frequency spectrum at $f = 0.31$, 0.63, 1.0, 1.26, and 2.07 (each falls into the 5 segments, respectively) under the two conditions are shown in Figs. 15 and 16, respectively.

The responses of the driveline with the wedge brake exhibit apparent stick motions at $f = 0.31$, 0.63, and

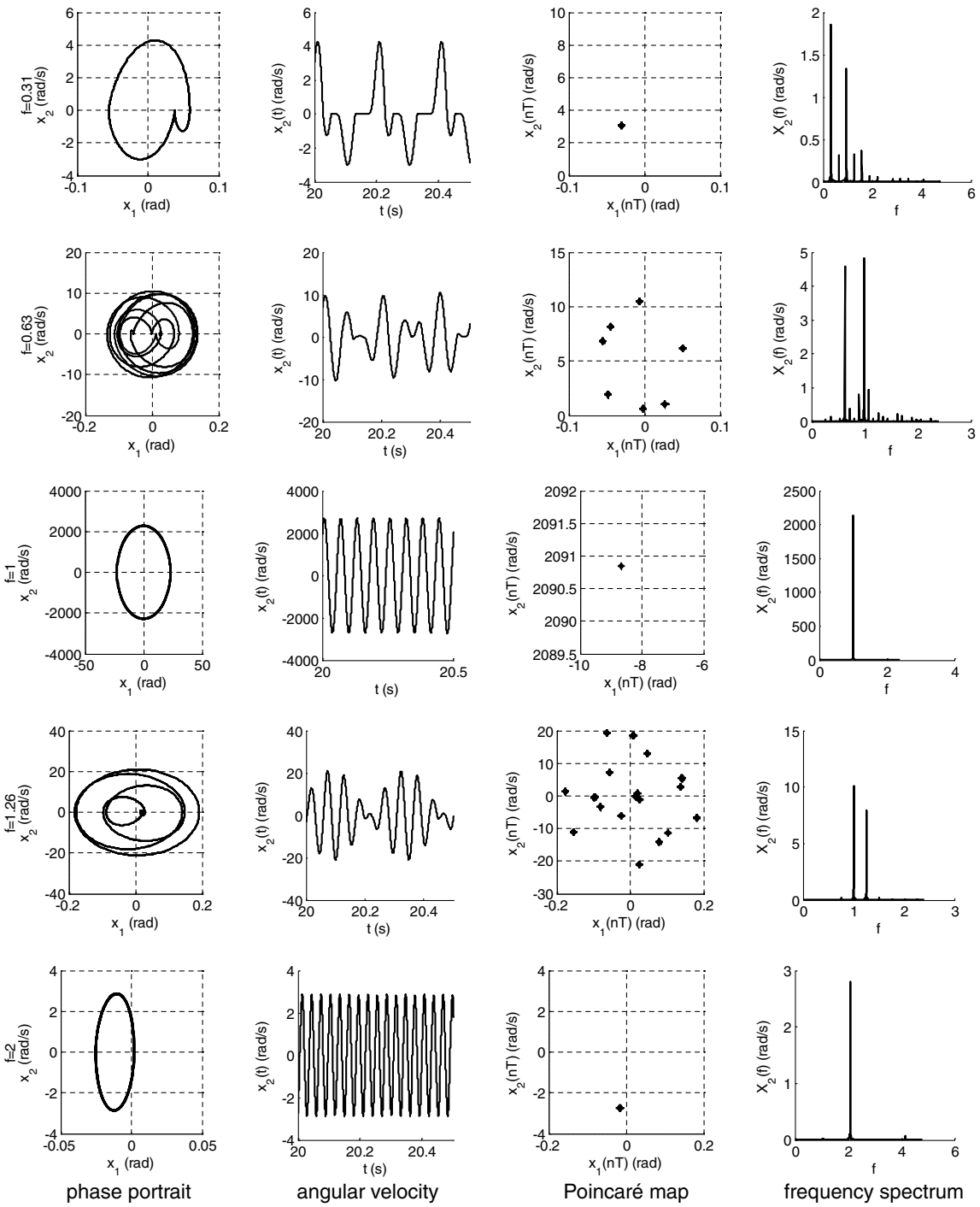

Fig. 15 Dynamic responses with different f at $\eta = -24$, $F_0 = 0.024$, $\alpha = 1.18$ for wedge brake

1.26; however, those with the conventional brake do not occur non-stop stick motion. The reason is that the friction force generated by the wedge brake is 12 times that by the conventional brake; therefore, more power is dissipated through the friction interface of the wedge brake.

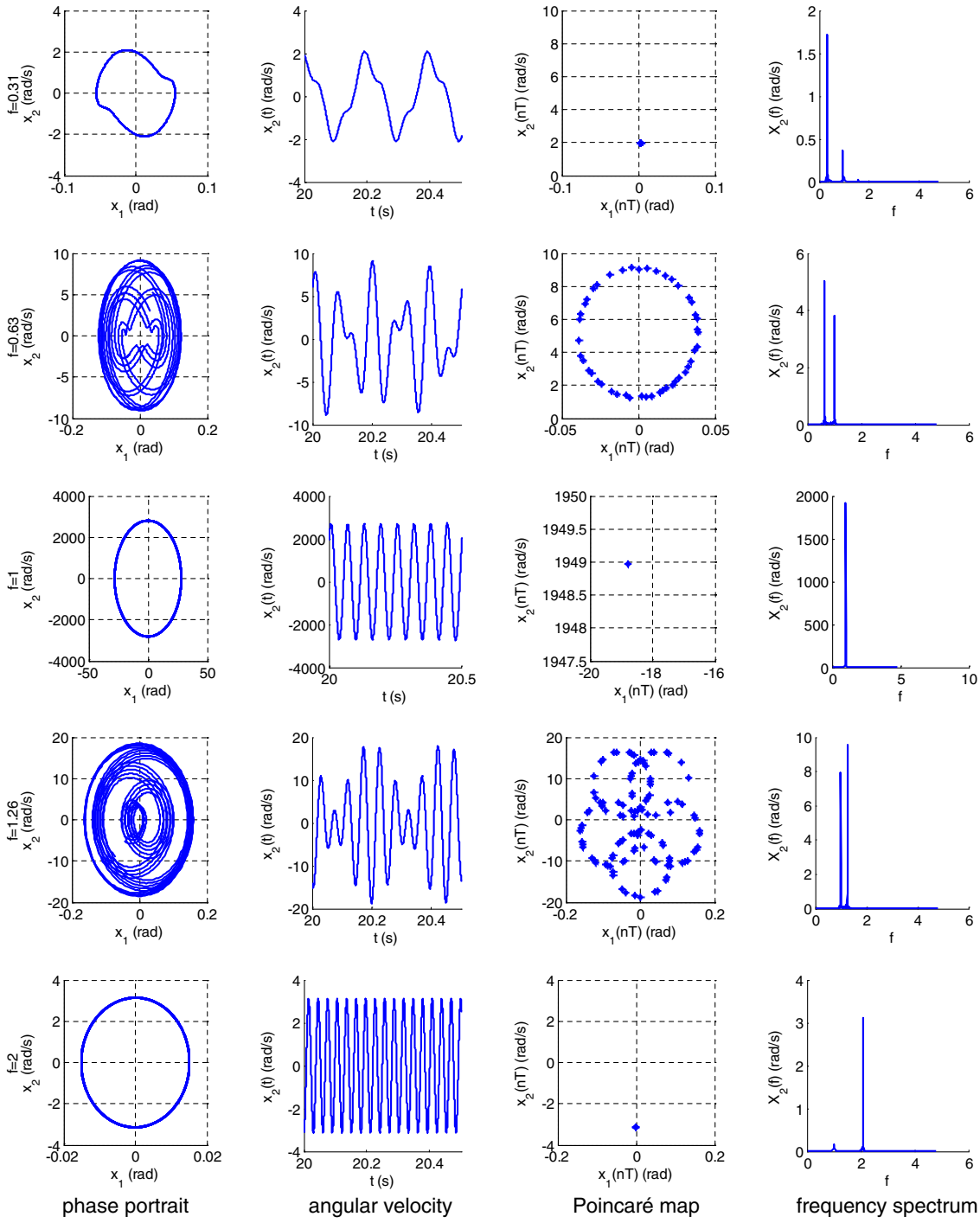

Fig. 16 Dynamic responses with different f at $\eta = -24$, $F_0 = 0.024$, $\alpha = 1.18$ for conventional brake

The Poincaré section maps of the multi-periodic motions at $f = 0.63$ and 1.26 for the wedge are rather irregular and have no symmetric axis. On the contrary, those for the conventional brake are more regular and come up with more than one symmetric axis.

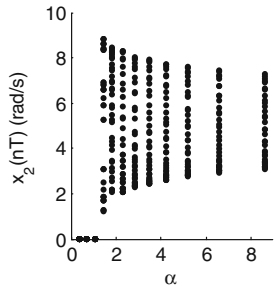

Fig. 17 Bifurcation diagrams of $x_2\,(nT)$ versus normalized wedge angle α

When $f < 1$, with an increasing f, the side bands of the driveline frequency spectra disappear gradually. And when f reaches the resonance frequency, i.e., $f = 1$, the driveline spectrum is neat only containing $f = 1$. After that, side bands occur in the multi-periodic motions until the response reaches synchronous motion at a large f in the fifth segment. On the other hand, as a whole, the frequency spectra for the conventional brake do not exhibit side bands as much as those for the wedge brake, because much less stick motions occur. Extremely, the spectra at $f = 1$ and at large f of the fifth segment are rather neat without side band.

4.5 Effect of α when $\eta < 0$

In this section, the normalized wedge angle α is selected as the bifurcation parameter. The value of α varies from 0.33 to 8.60, covering the possible range for the wedge brake design. Because the conventional brake is not associated with α, only the effect on the wedge brake is discussed in this section. With an increasing $\alpha$and other parameter constant, the bifurcation diagram is obtained as shown in Fig. 17.

It can be seen that the response evolution can be divided into 2 segments. The first segment exhibits synchronous motion at small $\alpha(0.33 \leq \alpha < 1.41)$. After that, the response transits to multi-periodic motion at large $\alpha(1.41 \leq \alpha < 8.60)$. The phase portraits, angular velocity, Poincaré map, and frequency spectrum at α =0.68 and 5.20 (each falls into the 2 segments, respectively) are shown in Fig. 18.

The driveline response exhibits unidirectional stick-slip motion at $\alpha = 0.68$. The reason is that a big friction force is generated, so the power from the excitation is quickly dissipated through the friction interface. At the same time, many side bands occur in the frequency spectrum.

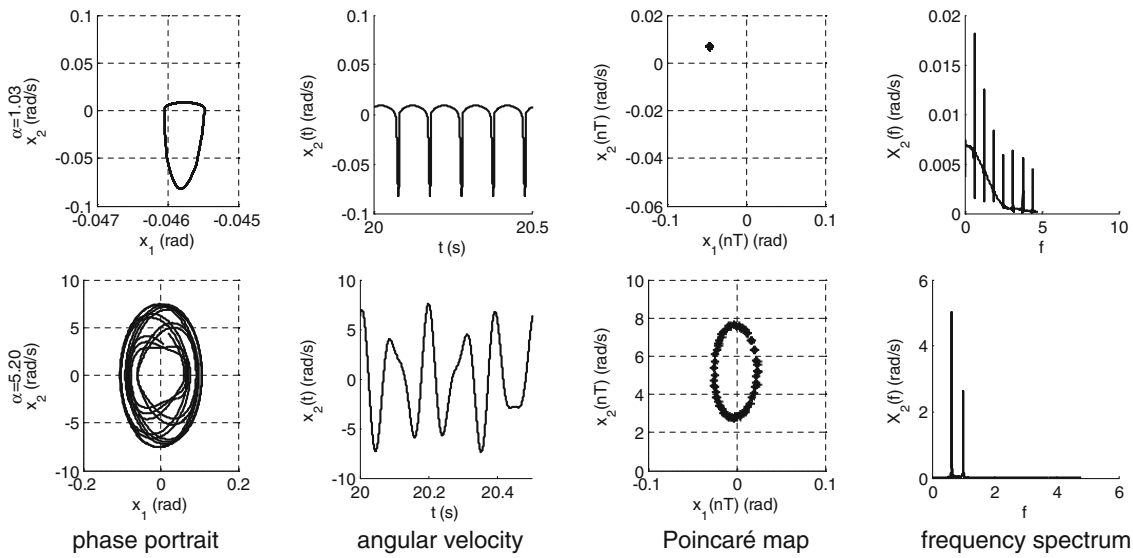

Fig. 18 Dynamic responses with different α at $f = 0.63$ $\eta = -24$, $F_0 = 0.024$ for wedge brake

When applying a large α, asymmetric response combined with stick-slip motions is observed at $\alpha = 5.20$. Because less friction force is generated at large α, less stick motions are induced. Resultantly, the frequency spectrum concentrates on the natural frequency and excitation frequency.

5 Conclusion

A SDOF torsional model with harmonic excitation for a driveline with a wedge brake is developed to investigate the effect of velocity-dependent actuation force. Stability analysis in terms of the slope of the actuation force η based on the linearized model is implemented, followed by nonlinear computation using smoothened friction characteristics. The results are provided by the comparison with the results of the driveline with a conventional brake.

The stability analysis indicates that instability can occur even with a constant friction coefficient, and is greatly influenced by η, no matter for the wedge brake or for the conventional brake. The critical η is associated with the friction coefficient μ_k and the wedge angle α for the wedge brake, however, is a constant as -1 for the conventional brake. Small μ_k or large α expands the stable area of the wedge brake. As a whole, positive η tends to fall into the stable area, whereas negative η to the unstable area. Three bifurcation points are found for the two brakes, respectively; among them one falls into the stable area, one into the unstable area, and the other one is a Hopf bifurcation point.

Phase portraits, time domain responses, Poincaré maps, and frequency spectra are obtained by nonlinear computation. Three typical motions are observed for the wedge brake, i.e., unidirectional stick-slip, bidirectional stick-slip, and non-stick slip, which demonstrate the asymmetric characteristics from the wedge. Due to the self amplification, the wedge brake leads to more stick motions compared with the conventional brake. Resultantly, more side bands occur.

Using the given parameters, the dynamic response of the driveline with the wedge brake is synchronous motion when $\eta > -18$; whereas multi-periodic motion when $\eta \leq -18$. Besides, the dynamic response is also affected by the initial actuation force F_0, excitation frequency f, and wedge angle α. For example, at $\eta = -24$, large $F_0 (F_0 > 0.044)$, extreme small or large $f (f > 0.3$ or $f > 1.57)$, and small $\alpha (\alpha < 1.41)$ outcome synchronous motions rather than the multi-periodic motions.

Acknowledgments The authors would like to thank Chinese National Science Foundation for the support on this project (Grant No. 51105244).

Appendix

The SDOF model of the driveline with a conventional brake is shown in Fig. 19. The actuation force F_a is acting as the normal force vertical to the friction interface.

The governing equation is

$$J\ddot{\theta}(t) + c\dot{\theta}(t) + k\theta(t) + RF_\mu(t) = T(t) \tag{21}$$

in which F_μ is described in Coulomb friction model as

$$F_\mu = \begin{cases} F_a \cdot \mu_k \cdot sign(\dot{\theta}(t)) & \dot{\theta}(t) \neq 0 \\ \left[-F_a \cdot \mu_s \;\; F_N \cdot \mu_s\right] & \dot{\theta}(t) = 0 \end{cases} \tag{22}$$

The system matrix **A** and input vector **U**are derived as

$$A = \begin{pmatrix} 0 & 1 \\ -\frac{k}{J} & -\frac{c}{J} - \frac{R\cdot\delta\cdot\mu_k}{J} \end{pmatrix}, \tag{23}$$

$$U = \begin{pmatrix} 0 \\ \frac{T(t) - R\cdot F_{a0}\cdot\mu_k\cdot sign(x_2(t))}{J} \end{pmatrix}. \tag{24}$$

The characteristic equation is

$$\det\begin{pmatrix} \lambda & -1 \\ \frac{k}{J} & \lambda + \frac{c}{J} + \frac{R\cdot\delta\cdot\mu_k}{J} \end{pmatrix} = 0. \tag{25}$$

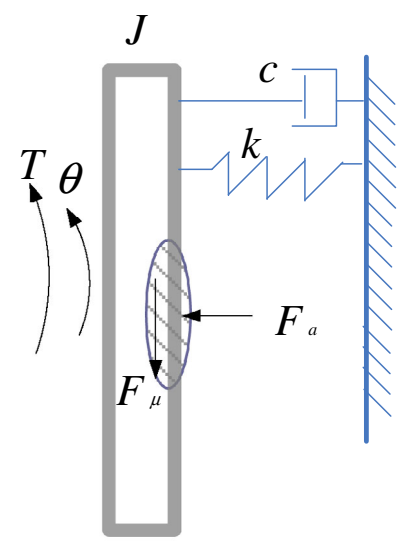

Fig. 19 Model of the driveline with a conventional brake

Define the natural frequency $\omega_n = \sqrt{k/J}$ and a symbol h as following, the solution of λ is calculated by

$$h = -\left(\frac{c}{2J} + \frac{R \cdot \delta \cdot \mu_k}{2J}\right) < 0 \tag{26}$$

$$\lambda = h \pm \sqrt{h^2 - \omega_n^2}. \tag{27}$$

Therefore, the asymptotically stable criterion is derived as

$$R \cdot \delta \cdot \mu_k / c > -1. \tag{28}$$

Replaced by the normalized parameter η, the criterion becomes

$$\eta > -1. \tag{29}$$

References

1. Akay, A., Giannini, O., Massi, F., Sestieri, A.: Disc brake squeal characterization through simplified test rigs. Mech.Syst. Signal Process. **23**(8), 2590–2607 (2009)
2. Sun, Z., Hebbale, K.: Challenges and opportunities in automotive transmission control. In: American control conference, Portland, OR, pp. 3284–3289. IEEE, New York (2005)
3. Roberts, R., Schautt, M., Hartmann, H., Gombert, B.: Modelling and validation of the mechatronic wedge brake. SAE Trans. **112**(6), 2376–2386 (2003)
4. Design, B., Chamfer, B.B.: ABS/ESC/EPB Control of Electronic Wedge Brake. SAE paper, 01–0074 (2010)
5. Ho, L.M., Roberts, R., Hartmann, H., Gombert, B.: The electronic wedge brake (EWB). SAE Pap. **620**, 01–3196 (2006)
6. Kim, J., Choi, S.B.: Design and modeling of a clutch actuator system with self-energizing mechanism. IEEE/ASME Trans. Mechatron. **16**(5), 953–966 (2011)
7. Yao, J., Chen, L., Yin, C., Shu, J., Zheng, X.: Modeling of a Wedge Clutch in an Automatic Transmission. SAE paper, 01–0186 (2010)
8. Awrejcewicz, J., Olejnik, P.: Analysis of dynamic systems with various friction laws. Appl. Mech. Rev. **58**(1/6), 389 (2005)
9. Cantoni, C., Cesarini, R., Mastinu, G., Rocca, G., Sicigliano, R.: Brake comfort—a review. Veh. Syst. Dyn. **47**(8), 901–947 (2009)
10. Stachowiak, G., Batchelor, A.W.: Engineering Tribology. Elseiver Butterworth–Heinemann, Burlington (2011)
11. Ouyang, H.: Moving-load dynamic problems: a tutorial (with a brief overview). Mech. Syst. Signal Process. **25**(6), 2039–2060 (2011)
12. Awrejcewicz, J., Grzelczyk, D.: Modeling and analytical/numerical analysis of wear processes in a mechanical friction clutch. Int. J. Bifurc. Chaos **21**(10), 2861–2869 (2011)
13. Pratt, E., Léger, A., Zhang, X.: Study of a transition in the qualitative behavior of a simple oscillator with Coulomb friction. Nonlinear Dyn. **74**(3), 517–531 (2013)
14. Awrejcewicz, J., Sendkowski, D.: Stick-slip chaos detection in coupled oscillators with friction. Int. J. Solids Struct. **42**(21), 5669–5682 (2005)
15. Zhang, X.-Q., Wang, X.-L., Zhang, Y.-Y.: Non-linear dynamic analysis of the ultra-short micro gas journal bearing-rotor systems considering viscous friction effects. Nonlinear Dyn. **73**, 751–765 (2013)
16. Pascal, M.: New limit cycles of dry friction oscillators under harmonic load. Nonlinear Dyn. **70**(2), 1435–1443 (2012)
17. Wen, G., Xu, G., Xie, J.: Controlling Hopf–Hopf interaction bifurcations of a two-degree-of-freedom self-excited system with dry friction. Nonlinear Dyn. **64**, 49–57 (2011)
18. Awrejcewicz, J., Olejnik, P.: Stick-slip dynamics of a two-degree-of-freedom system. Int. J. Bifurc. Chaos **13**(04), 843–861 (2003)
19. Gdaniec, P., Hoffmann, N.: On chaotic friction induced vibration due to rate dependent friction. Mech. Res. Commun. **37**(1), 92–95 (2010)
20. Fečkan, M.: Chaotic solutions in differential inclusions: chaos in dry friction problems. Trans. Am. Math. Soc. **351**(7), 2861–2873 (1999)
21. Sayed, M., Hamed, Y.: Stability and response of a nonlinear coupled pitch-roll ship model under parametric and harmonic excitations. Nonlinear Dyn. **64**, 207–220 (2011)
22. Wang, X., Mao, D., Wei, X., Li, J., Meng, H., Wang, W.: Sliding friction induced atom diffusion in the deformation layer of 0.45 % C steel rubbed against tin alloy. Tribology Int. **64**, 128–134 (2013)
23. Crowther, A., Zhang, N., Liu, D., Jeyakumaran, J.: Analysis and simulation of clutch engagement judder and stick-slip in automotive powertrain systems. Proc.Inst. Mech. Eng. D **218**(12), 1427–1446 (2004)
24. Chen, L., Xi, G., Yin, C.: Model referenced adaptive control to compensate slip-stick transition during clutch engagement. Int. J. Autom. Technol. **12**(6), 913–920 (2011)
25. Neubauer, M., Wallaschek, J.: Vibration damping with shunted piezoceramics: fundamentals and technical applications. Mech. Syst. Signal Process. **36**, 36–52 (2013)
26. Balogh, L., Streli, T., Nemeth, H., Palkovics, L.: Modelling and simulating of self-energizing brake system. Veh. Syst. Dyn. **44**, 368–377 (2006)
27. Saha, A., Bhattacharya, B., Wahi, P.: A comparative study on the control of friction-driven oscillations by time-delayed feedback. Nonlinear Dyn. **60**(1–2), 15–37 (2010)
28. Crowther, A., Singh, R.: Analytical investigation of stick-slip motions in coupled brake-driveline systems. Nonlinear Dyn. **50**(3), 463–481 (2007)
29. Franco, J., Franchek, M.A., Grigoriadis, K.: Real-time brake torque estimation for internal combustion engines. Mech. Syst. Signal Process. **22**(2), 338–361 (2008)
30. Cantone, F., Massi, F.: A numerical investigation into the squeal instability: effect of damping. Mech. Syst. Signal Process. **25**(5), 1727–1737 (2011)
31. Oberst, S., Lai, J., Marburg, S.: Guidelines for numerical vibration and acoustic analysis of disc brake squeal using simple models of brake systems. J.Sound Vib. **332**, 2284–2299 (2013)
32. Duan, C., Singh, R.: Dynamics of a 3DOF torsional system with a dry friction controlled path. J.Sound Vib. **289**(4–5), 657–688 (2006)
33. Martinez, R., Alvarez, J.: A controller for 2-DOF underactuated mechanical systems with discontinuous friction. Nonlinear Dyn. **53**(3), 191–200 (2008)

34. Andreaus, U., Casini, P.: Dynamics of friction oscillators excited by a moving base and/or driving force. J.Sound Vib. **245**(4), 685–699 (2001)
35. Hetzler, H., Schwarzer, D., Seemann, W.: Analytical investigation of steady-state stability and Hopf-bifurcations occurring in sliding friction oscillators with application to low-frequency disc brake noise. Commun. Nonlinear Sci.Numer. Simul. **12**(1), 83–99 (2007)
36. Li, Y., Feng, Z.: Bifurcation and chaos in friction-induced vibration. Commun. Nonlinear Sci.Numer. Simul. **9**(6), 633–647 (2004)
37. Awrejcewicz, J., Grzelczyk, D., Pyryev, Y.: 404. A novel dry friction modeling and its impact on differential equations computation and Lyapunov exponents estimation. J. Vibroeng. **10**(4) (2008)
38. Duan, C., Singh, R.: Transient responses of a 2-dof torsional system with nonlinear dry friction under a harmonically varying normal load. J. Sound Vib. **285**(4–5), 1223–1234 (2005)